High-Frequency High-Efficiency GaN-Based Interleaved CRM Bidirectional Buck/Boost Converter with Inverse Coupled Inductor

Xiucheng Huang, *Student Member, IEEE*, Fred C. Lee, *Life Fellow, IEEE*, Qiang Li, *Member, IEEE*, and Weijing Du

***Abstract*—This paper presents a high-frequency high-efficiency GaN device-based interleaved critical current mode (CRM) bidirectional buck/boost converter with an inverse coupled inductor. The switching frequency is continually driven to megahertz range with GaN devices due to their small switching loss and driving loss, which greatly reduces the size of the passive components. The coupled inductor further reduces the core volume due to certain dc flux reductions. The equivalent inductance and the impact of the inverse coupled inductor on the CRM buck–boost converter are analyzed in detail. The resonant period in CRM is less with an inverse coupled inductor than with a noncoupled inductor, which is beneficial for the high-frequency operation. The soft-switching range and the circulating energy are both improved using an inverse coupled inductor in CRM. Experimental results validate the theoretical analysis, and the coupled inductor prototype efficiency is 98.5% at 1 MHz, which is 0.3% higher than a prototype with a noncoupled inductor.**

***Index Terms*—Bidirectional converter, critical current mode (CRM), gallium nitride (GaN), interleaving, inverse coupled inductor, zero-voltage switching (ZVS).**

I. Introduction

THE bidirectional buck/boost converter is widely used in the power electronics system due to its simplicity and high efficiency, such as the on board charger/discharger for plug-in hybrid electric vehicles [1]–[3], and the interfaced converter for the energy storage systems [4], [5]. Conventional silicon device-based bidirectional buck/boost converters are usually intended to be operated in discontinuous-current mode (DCM) in order to alleviate reverse recovery issues and to use a small inductor. However, the DCM operation greatly increases turn-off loss because the main switch is turned-off at least twice of the load current. As a result, the switching frequency can barely be pushed to hundreds of kilohertz due to power loss considerations.

In recent years, the GaN devices have emerged as promising devices for high frequency, high efficiency, and high density power conversion due to a better figure of merit than comparable Si and SiC transistors [6], [7]. The switching frequency of GaN devices has been continuously pushed up to several megahertz to both reduce the size of the passive components and to increase power density [8]–[11]. Huang *et al.* [12]–[14] have thoroughly illustrated the switching loss mechanism in a high-voltage cascode GaN switch and derived two important switching characteristics. One is that the turn-on switching loss is dominant due to the reverse recovery charge or junction capacitor charge of the free-wheeling device at hard-switching condition. The other notable characteristic is that the turn-off loss is negligible because of the intrinsic current source driving mechanism in cascode structure. These important switching characteristics imply that zero-voltage switching (ZVS) is still desired for GaN devices in high-frequency applications, while the turn-off current is no longer a big concern for cascode GaN devices. Huang *et al.* [13, Figs. 16 and 17] clearly show the efficiency and loss distribution comparison between a cascode GaN switch and Si MOSFET under soft-switching conditions. The experiment data validate the advantages of GaN devices.

Critical current mode (CRM) operation is the most simple and effective way to achieve ZVS, and is widely used in medium-low power applications [8], [11], [13]. CRM operation introduces a large current ripple, which is at least twice of the load current. It is necessary to interleave multiple phases to cancel the switching frequency current ripple and lead to a smaller EMI filter. However, the ZVS range of the CRM dc–dc converter is determined by the input and output voltage, which will significantly impact switching loss at high frequency. Furthermore, the resonant period formed by the inductor and device junction capacitors is too long at high frequency, which leads to a large circulating energy. The limitations of CRM operation at high frequency are discussed in Section II.

The concept of the coupled inductor has been applied successfully in interleaved voltage regular modules for the improvement of the efficiency and transient response [15]. The inverse coupled inductor has also been evaluated in the interleaved CRM boost PFC converter which aims to reduce the magnetic volume [16]. However, the impact of the coupled inductor on the behavior of the converter during the resonant period, which is unique to CRM operation, has not yet been analyzed.

This paper aims to analyze the behavior of interleaved buck/boost converter with an inverse coupled inductor operating in CRM. The derivation of the equivalent inductance of the inverse coupled inductor in CRM is illustrated in Section III. The benefits of the inverse coupled inductor in CRM are analyzed in Section IV, including resonant period reduction, and

Manuscript received April 8, 2015; revised July 25, 2015; accepted August 31, 2015. Date of publication September 3, 2015; date of current version January 7, 2016. This work was supported by the Power Management Consortium in the Center for Power Electronics Systems, Virginia Polytechnic Institute and State University. Recommended for publication by Associate Editor V. Agarwal.

The authors are with the Center for Power Electronics Systems, The Bradley Department of Electrical and Computer Engineering, Virginia Polytechnic Institute and State University, Blacksburg, VA 24061 USA (e-mail: xiucheng@vt.edu; fclee@vt.edu; lqvt@vt.edu; weijing@vt.edu).

Color versions of one or more of the figures in this paper are available online at http://ieeexplore.ieee.org.

Digital Object Identifier 10.1109/TPEL.2015.2476482

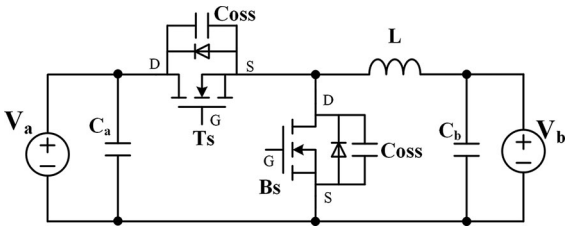

Fig. 1. Bidirectional buck/boost converter.

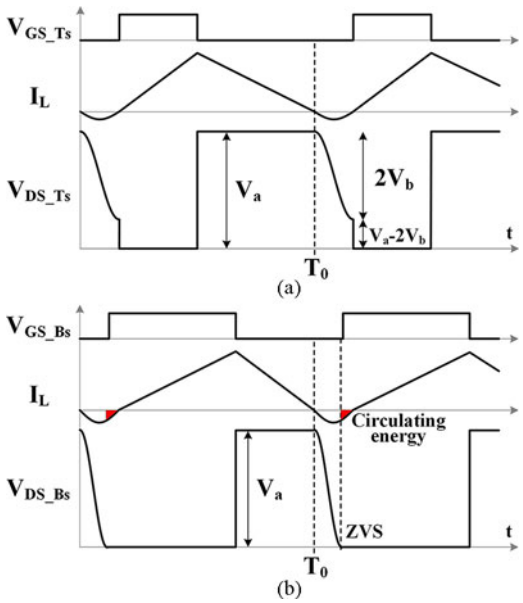

Fig. 2. Key waveforms of CRM operation for buck/boost converter. (a) Buck direction. (b) Boost direction.

an improvement in ZVS range and circulating energy. Finally, the theoretical analysis is validated by experimental results.

II. Limitations of CRM Operation at High Frequency

When the bidirectional buck/boost converter, which is shown in Fig. 1, operates in CRM, it can achieve zero current turn-on for the main switch and zero current turn-off of the freewheeling switch, thus avoiding reverse recovery problems. Switch T_s is the main switch in the buck direction, while B_s is the main switch in the boost direction. If the main switch turn-on instant is set to exactly half the resonant period after the inductor current crosses zero via any zero-current detection technique, the switch achieves minimum voltage turn-on. Fig. 2 shows the key CRM operation waveforms for both buck operation and boost operation.

v_{DST} and v_{DSB} are the drain-source voltage of T_s and B_s, respectively. The inductor current crosses zero at t_0 and then the inductor oscillates with the junction capacitors of the two devices. It is easy to derive the voltage oscillation peak-to-peak amplitude for both directions, which is $2 * V_b$ for the buck direction and $2 * (V_a - V_b)$ for the boost direction. Fig. 2 shows a 380 to 150 V conversion as an example. The main switch T_s is turned ON at the valley point, which is 80 V $(V_a - 2 * V_b)$ in the buck direction. The main switch B_s in the boost direction can

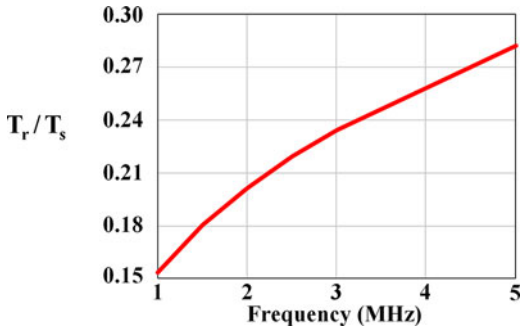

Fig. 3. Relationship between T_r and T_s in CRM.

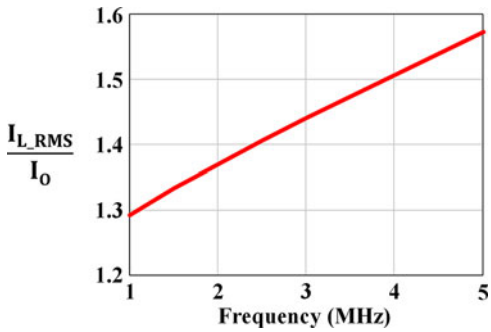

Fig. 4. Inductor current rms value increases with frequency in CRM.

easily achieve ZVS since the resonant amplitude $2 * (V_a - V_b)$ is larger than the device initial voltage, which is V_a. The extra circulating energy is marked by the red shadow region Therefore, one direction will lose ZVS and the other direction will have extra circulating energy except for the special case where V_a is exactly twice V_b. The switching loss and circulating energy will increase with the frequency, which will deteriorate the efficiency significantly at high frequency.

Another limiting factor of CRM operation at high frequency is the resonant time T_r, which is half of the resonant period formed by L and the junction capacitors of the devices, which is expressed as

$$T_r = \pi \cdot \sqrt{L \cdot 2C_{OSS}}. \tag{1}$$

During the resonant period, the charge stored in the junction capacitor of the main switch is recycled to the source, while the same amount of charge is stored in the junction capacitor of the freewheeling switch. Therefore, the negative charge of the inductor current, which does not transfer energy to the output, is constant no matter what the switching frequency is. Fig. 3 shows the trend that T_r/T_s increases with the switching frequency. As a result, the rms value of the inductor current will increase with the switching frequency as shown in Fig. 4, whereas the output current remains same at different switching frequency. Both of these two curves are derived from simulation. At 5 MHz, the resonant period occupies 28% of the total switching period, and the rms value of inductor current is 1.57 times the output current. Fig. 5 shows a 5-MHz experiment waveform with the resonant period clearly marked.

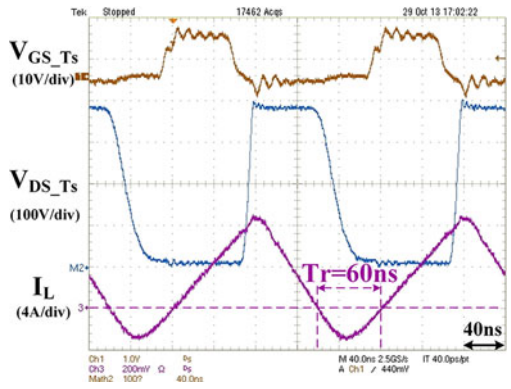

Fig. 5. CRM operation experimental waveforms at 5 MHz.

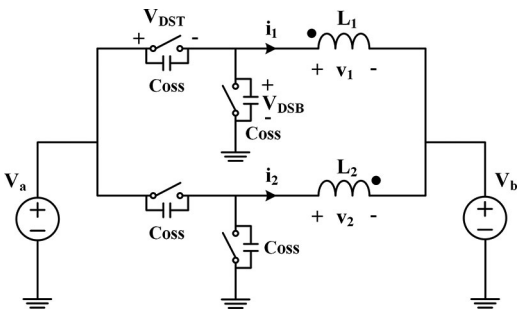

Fig. 6. Interleaved buck/boost converter with inverse coupled inductor.

One way to solve the limitations of conventional CRM operation is to utilize the quasi-square-wave soft-switching technique [3], [5], [17], [18]. However, the negative portion of the inductor current grows larger under light-load conditions, which will significantly deteriorate the converter efficiency. Another solution is to use a coupled inductor to improve the CRM performance, including ZVS range extension/circulating energy reduction and resonant period reduction. This process is analyzed in detail in Sections III and IV.

III. Equivalent Inductance Derivation at CRM

The interleaved bidirectional buck/boost converter with an inverse coupled inductor is shown in Fig. 6. For simplicity, the two self-inductances are considered to be the same ($L_1 = L_2 = L$). The inverse coupled mutual inductance *M* is expressed as

$$M = k \cdot L, \quad k < 0 \tag{2}$$

where *k* is the coupling coefficient.

The analysis of the inverse coupled inductor in continuous-current mode (CCM) operation is illustrated in [15]. For CRM operation, there are two more resonant periods in each switching cycle than in CCM operation. The derivation of the equivalent inductance in CRM operation is shown below. The analysis of boost direction is a duplicate of the buck direction analysis.

The key waveforms for $D < 0.5$ are shown in Fig. 7(a), where *D* is the duty cycle. For the buck direction, $D = V_b/V_a$. There are six time intervals in one switching cycle. The time intervals $t_0 - t_1$, $t_1 - t_2$, $t_3 - t_4$, and $t_4 - t_5$ are the same with a

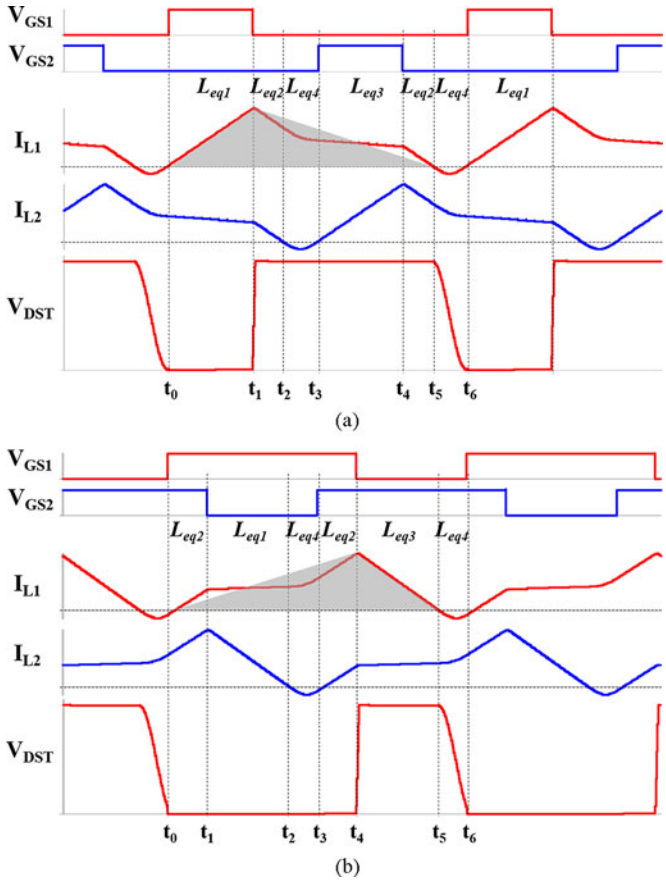

Fig. 7. Key waveforms of CRM with coupled inductor considering resonant period. (a) $D < 0.5$. (b) $D > 0.5$.

TABLE I
Coupled Inductor Equivalent Inductance [15]

L_{eq1}	L_{eq2}	L_{eq3}
$\frac{L^2-M^2}{L+\frac{D}{D'}M}$	$(L+M)$	$\frac{L^2-M^2}{L+\frac{D'}{D}M}$

*$D' = 1 - D$.

conventional two-phase buck converter with a coupled inductor. The time intervals $t_2 - t_3$ and $t_5 - t_6$ are the resonant periods that are different from the previous analysis. The derivation of the equivalent inductance during $t_0 - t_1$, $t_1 - t_2$, $t_3 - t_4$, and $t_4 - t_5$ can be found in [15], which is summarized in Table I. This paper focuses on analyzing the coupled inductor behavior during the resonant period.

The basic equation for the coupled inductor is

$$\begin{cases} v_1 = L \cdot \dfrac{di_1}{dt} + M \cdot \dfrac{di_2}{dt} \\ v_2 = L \cdot \dfrac{di_2}{dt} + M \cdot \dfrac{di_1}{dt} \end{cases} \tag{3}$$

where v_1, v_2 and i_1, i_2 are as marked in Fig. 6.

During t_5 to t_6, the Phase 1 inductor current drops to zero, and then, resonates with the junction capacitors of the two devices, while the Phase 2 inductor is still freewheeling through the bottom switch. The voltage across the two inductors can be

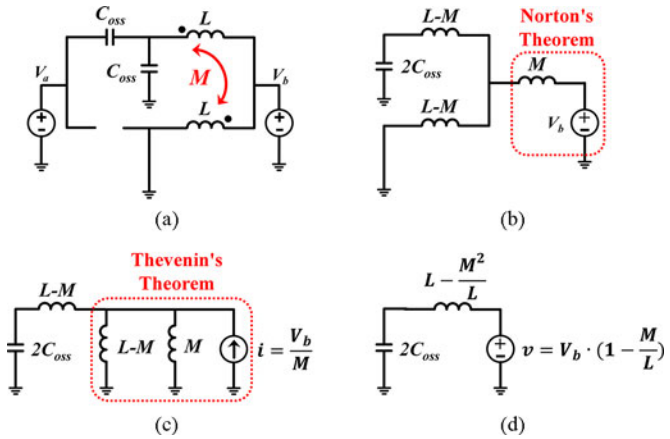

Fig. 8. Equivalent inductance derivation via equivalent circuit at $D < 0.5$. (a) Initial circuit during resonant period. (b) Decoupled inductor. (c) Circuit derivation with Norton's Theorem. (d) Circuit derivation with Thevenin's Theorem.

expressed as

$$v_1 = v_{\mathrm{DSB}} - V_b,\ v_2 = -V_b. \tag{4}$$

Meanwhile, the Phase 1 inductor current is related to the charge and discharge current of the two junction capacitors, which can be expressed as

$$i_1 = -2C_{OSS} \cdot \frac{dv_{\mathrm{DSB}}}{dt}. \tag{5}$$

Substituting v_1, v_2, and i_1 into (3), then (3) can be rewritten as follows:

$$\left(L - \frac{M^2}{L}\right) \cdot 2C_{OSS} \cdot \frac{d^2 v_{\mathrm{DSB}}}{dt^2} + v_{\mathrm{DSB}} = V_b \left(1 - \frac{M}{L}\right). \tag{6}$$

This is a two-order system from which we can define the equivalent resonant inductance mathematically as

$$L_{\mathrm{eq4}} = L - \frac{M^2}{L}. \tag{7}$$

To better understand the meaning of the equivalent resonant inductance, the derivation process based on the equivalent circuit is also demonstrated in Fig. 8. Fig. 8(a) shows the original circuit with a coupled inductor during the resonant period. Fig. 8(b) shows the equivalent circuit with decoupled inductors. The voltage source V_a is neglected since it only impacts the initial value. Based on Norton's theorem, the voltage source V_b in series with the inductor M can be replaced by a current source in parallel with an inductor as shown in Fig. 8(c). Then based on Thevenin's Theorem, the current source in parallel with an inductor can be represented as a voltage source in series with an inductor, as shown in Fig. 8(d). Therefore, the equivalent inductance derived from the circuit is same with mathematic derivation.

The aforementioned equivalent inductance derivation is focused on Phase 1. Following the same process, the equivalent inductance for Phase 2 can also be obtained. Even though the Phase 2 is on the freewheeling period, the resonant current in Phase 1 will be reflected to Phase 2 due to the coupling effect. Therefore, the current waveform of Phase 2 shown in Fig. 7(a) during $t_5 - t_6$ is a part of the sinusoid shape.

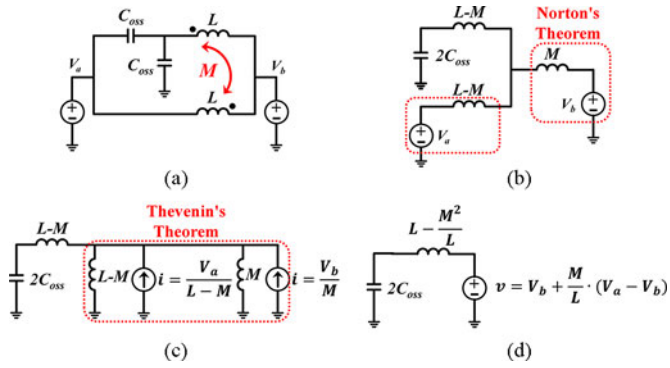

Fig. 9. Equivalent inductance derivation via equivalent circuit at $D > 0.5$. (a) Initial circuit during resonant period. (b) Decoupled inductor. (c) Circuit derivation with Norton's Theorem. (d) Circuit derivation with Thevenin's Theorem.

According to (6), the voltage waveform v_{DST} during the resonant period could be derived as follows:

$$v_{\mathrm{DST}} = V_a - V_b \cdot \left(1 - \frac{M}{L}\right) \cdot \times \left[1 - \cos\left(\frac{t}{\sqrt{\left(L - \frac{M^2}{L}\right) \cdot 2C_{OSS}}}\right)\right]. \tag{8}$$

It is evident that the resonant amplitude is related to the mutual inductance. Therefore, the inverse coupled inductor modifies the converter behavior in CRM.

The same process can be applied when $D > 0.5$. The key waveforms for the $D > 0.5$ condition are shown in Fig. 7(b). The equivalent circuit is shown in Fig. 9 with detailed derivation steps. The equivalent inductance during resonant period is also $L - \frac{M^2}{L}$ when $D > 0.5$. The voltage v_{DST} can be derived as

$$v_{\mathrm{DST}} = V_a - \left[V_b + \frac{M}{L} \cdot (V_a - V_b)\right] \cdot \times \left[1 - \cos\left(\frac{t}{\sqrt{\left(L - \frac{M^2}{L}\right) \cdot 2C_{\mathrm{OSS}}}}\right)\right]. \tag{9}$$

The derivation of the equivalent inductance in the boost direction is identical to the process of the buck direction, which will not be repeated here. The key equation to describe v_{DSB} during the resonant period is shown below. It indicates that the equivalent resonant inductance for the boost direction is also $L - \frac{M^2}{L}$ eqn. (10) at the bottom of the next page.

Table II summarizes the major difference between the non-coupled and inverse coupled inductors for both directions. The impact of the coupled inductor on the CRM operation is analyzed in Section IV.

TABLE II
COMPARISON BETWEEN NONCOUPLED INDUCTOR AND INVERSE COUPLED INDUCTOR

	Resonant inductance		Resonant amplitude		
	Noncoupled	Inverse coupled	Noncoupled	Inverse coupled	
Buck	L	$L-\frac{M^2}{L}$	V_b	$V_b<0.5V_a$ $V_b\cdot(1-\frac{M}{L})$	$V_b>0.5V_a$ $V_b+\frac{M}{L}\cdot(V_a-V_b)$
boost	L	$L-\frac{M^2}{L}$	V_a-V_b	$V_a-V_b\cdot$ $(1-\frac{M}{L})$	$(V_a-V_b)\cdot$ $(1-\frac{M}{L})$

IV. BENEFITS OF THE INVERSE COUPLED INDUCTOR AT CRM OPERATION

A. Reduction of Resonant Period

As shown in Fig. 7(a), the current decay slope is the same during $[t_1-t_2]$ and $[t_4-t_5]$, and the time intervals of $[t_1-t_2]$ and $[t_4-t_5]$ are the same, so the area between the current waveform and the time axis is equal to the shaded area. This principle also is true when $D>0.5$, which is shown in Fig. 7(b). Hence, same as the noncoupled case, the peak current of each phase of the coupled inductor is approximately twice of its average value, if the negative current is ignored.

For the coupled inductor case, it is apparent that $L_{\rm eq1}$ and $L_{\rm eq3}$ determine the peak value of the inductor current when $D<0.5$ and $D>0.5$, respectively. For a noncoupled inductor, each phase inductance L_{nc} determines the peak inductor current. To get the same average inductor current, $L_{\rm eq1}$ and $L_{\rm eq3}$ should be the same as L_{nc} when $D<0.5$ and $D>0.5$, respectively, which is expressed as follows:

$$\begin{cases} L_{nc}=L_{\rm eq1}=L\cdot\dfrac{1-k^2}{1+\dfrac{D}{D'}k}, & D<0.5 \\ L_{nc}=L_{\rm eq3}=L\cdot\dfrac{1-k^2}{1+\dfrac{D'}{D}k}, & D>0.5. \end{cases} \tag{11}$$

As the equivalent resonant inductance with a coupled inductor is $L_{\rm eq4}=L-\frac{M^2}{L}$ which can be rewritten as $L_{\rm eq4}=L(1-\alpha^2)$, the relation between $L_{\rm eq4}$ and L_{nc} can be expressed as:

$$\begin{cases} L_{\rm eq4}=L_{nc}\cdot\left(1+\dfrac{D}{D'}k\right), & D<0.5 \\ L_{\rm eq4}=L_{nc}\cdot\left(1+\dfrac{D'}{D}k\right), & D>0.5. \end{cases} \tag{12}$$

The inverse coupling coefficient k is negative which means the equivalent resonant inductance of a coupled inductor is always smaller than a noncoupled inductor. As shown in Fig. 10, the equivalent resonant inductance decreases with the coupling coefficient and reaches the lowest value when $D=0.5$. Accordingly, the resonant period with coupled inductor is also reduced compared to noncoupled case as shown in Fig. 11.

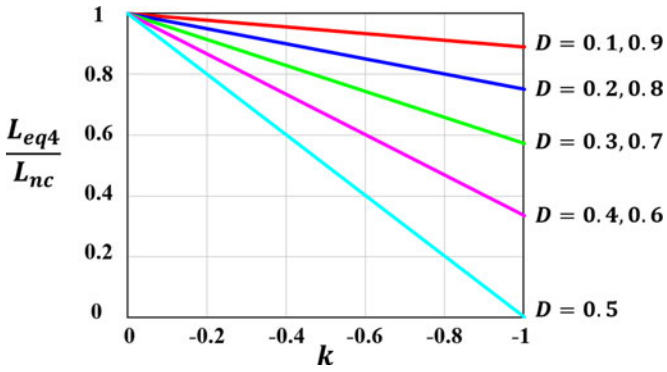

Fig. 10. Reduction of resonant inductance with different coupling coefficient and voltage gain.

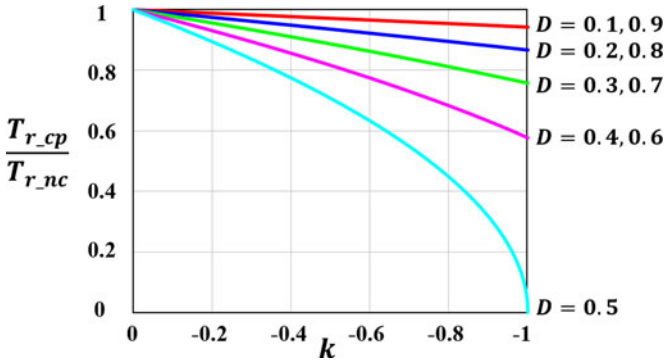

Fig. 11. Reduction of resonant period with different coupling coefficient and voltage gain.

$$\begin{cases} v_{\rm DSB}=V_a-\left[V_a-V_b\cdot\left(1-\dfrac{M}{L}\right)\right]\cdot\left[1-\cos\left(\dfrac{t}{\sqrt{\left(L-\dfrac{M^2}{L}\right)\cdot 2C_{OSS}}}\right)\right], & \dfrac{V_b}{V_a}<0.5 \\ v_{\rm DSB}=V_a-(V_a-V_b)\cdot\left(1-\dfrac{M}{L}\right)\cdot\left[1-\cos\left(\dfrac{t}{\sqrt{\left(L-\dfrac{M^2}{L}\right)\cdot 2C_{OSS}}}\right)\right], & \dfrac{V_b}{V_a}>0.5. \end{cases} \tag{10}$$

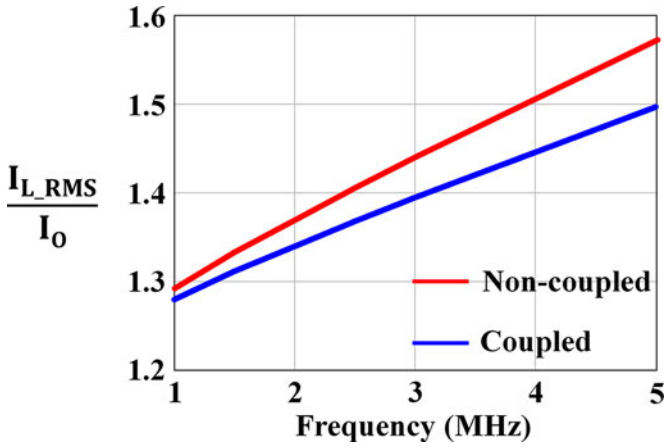

Fig. 12. Reduction of inductor current rms value with coupled inductor.

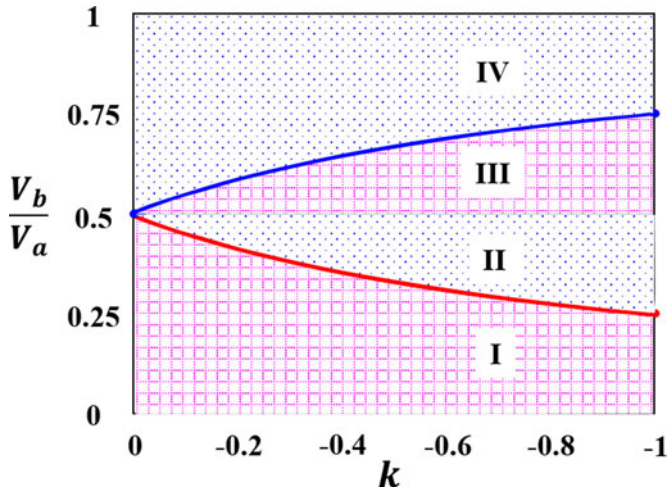

Fig. 13. Coupled inductor modifies CRM operation.

The portion of transferring energy increases with the reduction of the resonant period in CRM, which leads to a reduction of conduction loss. Fig. 12 shows the theoretical calculation results of the rms value reduction of the inductor current when $D = 0.6, k = -0.4$. The bottom curve shows a 5% reduction of inductor current when using a coupled inductor rather than a noncoupled inductor at 5 MHz, as well as a 10% reduction of the converter conduction loss.

B. Extension of ZVS Range when $D < 0.5$ or Reduction of Circulating Energy When $D > 0.5$

For a bidirectional buck/boost converter with a noncoupled inductor operating in CRM, one of the directions operates at $D < 0.5$ and switches at the valley point, as shown in Fig. 2(a), while the other direction operates at $D > 0.5$ and can achieve ZVS easily with extra circulating energy. Even valley switching minimizes the turn-on switching loss, the remaining energy stored in the junction capacitor is still considerable at megahertz switching frequency. A similar argument can also be applied to the circulating energy as this a part of the power loss is a linear function of the switching frequency.

However, the inverse coupled inductor can modify the converter behavior during the resonant period. As shown in Table II in Section III, the resonant amplitude with an inverse coupled inductor is different from the resonant amplitude with a noncoupled inductor. Taking a $V_a = 380$ V, and $V_b = 150$ V conversion as an example, in the buck direction, ZVS cannot be achieved with a noncoupled inductor operating in CRM since V_b is smaller than 0.5 V_a. However, ZVS can be achieved with an inverse coupled inductor as long as the coupling coefficient is in the range of $-1 < k < -0.3$ and makes $V_b \cdot (1 - k)$ greater than 0.5 V_a. In the boost direction, ZVS can be easily achieved with a noncoupled inductor with extra circulating energy since the resonant amplitude $V_a - V_b$ is greater than 0.5 V_a. While the coupled inductor reduces the resonant amplitude to $\left[V_a - V_b \cdot \left(1 - \frac{M}{L}\right)\right]$. ZVS still can be achieved as long as k is in the range of $-1 < k < -0.3$. Therefore, designing coupling coefficient to be around -0.3 is the most beneficial for both directions.

Fig. 13 summarizes the benefit of the ZVS range extension and circulating energy reduction with an inverse coupled inductor. The solid line is the ZVS boundary condition, which is the most desired operation point. Regions I and III represent the valley switching for the buck direction, while they represent ZVS with circulating energy for the boost direction. Regions II and IV represent ZVS with circulating energy for the buck direction but valley switching for the boost direction. If the operation point is close to the ZVS boundary line, there is smaller turn-on switching loss in one direction and smaller circulating energy in the other direction.

For the noncoupled inductor case, the only ZVS boundary point for both directions is $\frac{V_b}{V_a} = 0.5$. For the inverse coupled inductor case, the ZVS boundary is stretched to two lines. When the voltage gain ratio $\frac{V_b}{V_a}$ is between 0.25 and <0.75, the operation point can be located on the ZVS boundary line at certain coupling coefficients, as shown in Fig. 13. When $\frac{V_b}{V_a}$ is $\langle 0.25 \text{ or} > 0.75 \rangle$, the operation point moves to Regions I and IV. However, the operation point is much closer to the ZVS boundary line than in the noncoupled condition. This indicates a reduction of turn-on switching loss and circulating energy. Over all, the inverse coupled inductor improves the converter performance in CRM operation.

When apply inverse coupled inductor in high-frequency two-phase interleaved CRM PFC converter, the aforementioned benefits will definitely improve the converter efficiency. Take the two-phase CRM totem-pole PFC, which is discussed in [8], as an example. The non-ZVS valley switching is inevitable with noncoupled inductor when the input voltage is higher than half of the output voltage, which causes a considerable switching loss at high frequency. On the other hand, ZVS could be easily achieved with extra circulating current when the input voltage is lower than half of the output voltage, which causes the additional conduction loss. With an inverse coupled inductor, the non-ZVS valley switching region will be narrowed and the circulating current would be reduced since the operation point is moving closer to the ZVS boundary line as illustrated in Fig. 13. Therefore, it takes less effort to achieve ZVS by operating at QSW

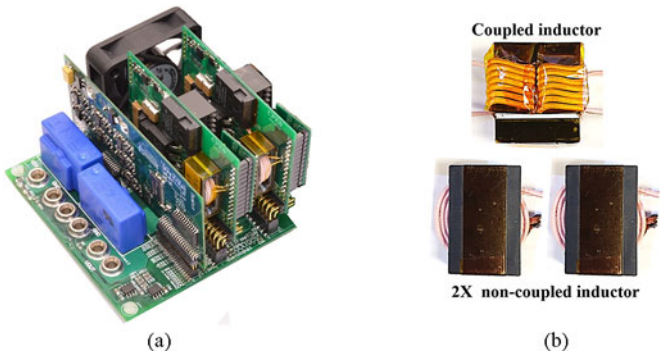

Fig. 14. Prototype and inductor comparison. (a) Two-phase interleaved buck/boost converter prototype. (b) Comparison of coupled and noncoupled inductor.

mode [8]. Moreover, QSW mode cannot solve the circulating current problem.

V. Experimental Results and Discussions

To validate the benefit of the converter operating in CRM with inverse coupled inductor, a 380–150-V two-phase interleaved CRM buck/boost converter is built. The output current is 8 A for the buck direction and 3 A for the boost direction. The converter can operate with both an inverse coupled inductor and a noncoupled inductor for comparison. The 600-V GaN HEMT from Transphorm is used as the active switch, since the turn-off switching loss is negligible, which means it is suitable for CRM operation and can be pushed to a very high frequency. The switching frequency is set to be 1 MHz at full-load condition to reduce the size of the passive components. An UI-shaped core with 3F45 material is used in the prototype, and the air gap is fine tune to achieve a certain coupling coefficient. Two ER23 core with 3F45 material are used as the noncoupled inductors for comparison. The prototype is shown in Fig. 14. The coupled inductor saves 50% footprint and 25% volume compared with two noncoupled inductors. The design and optimization of the coupled inductor is a complex process which is not addressed in this paper. The experiments shown below only focus on the theoretical analysis illustrated in Sections III and IV.

The steady-state inductance for the noncoupled inductor is 8 μH, and determines the peak current and output current. For the inverse coupled inductor case, L_{eq1} and L_{eq3} determine the peak and average values of the inductor current in the buck direction and boost direction, respectively. The Table I shows the relationship between these two inductors and the self-inductance, coupling coefficient, and duty cycle. In the prototype, the self-inductance is 8 μH, and the coupling coefficient is -0.4.

Fig. 15 shows the bidirectional waveforms with a noncoupled inductor. The detailed waveforms during the resonant period for the buck and boost direction are shown in Fig. 15(b) and (d), respectively. As the voltage conversion ratio has been set from 380 to 150 V, the buck direction loses ZVS and the boost direction achieves ZVS with extra circulating energy, as marked in the figure. In the buck direction, the main switch is turned on at 80 V, which means there is an approximately 1 W turn-on switching loss at 1 MHz. In the boost direction, the circulating

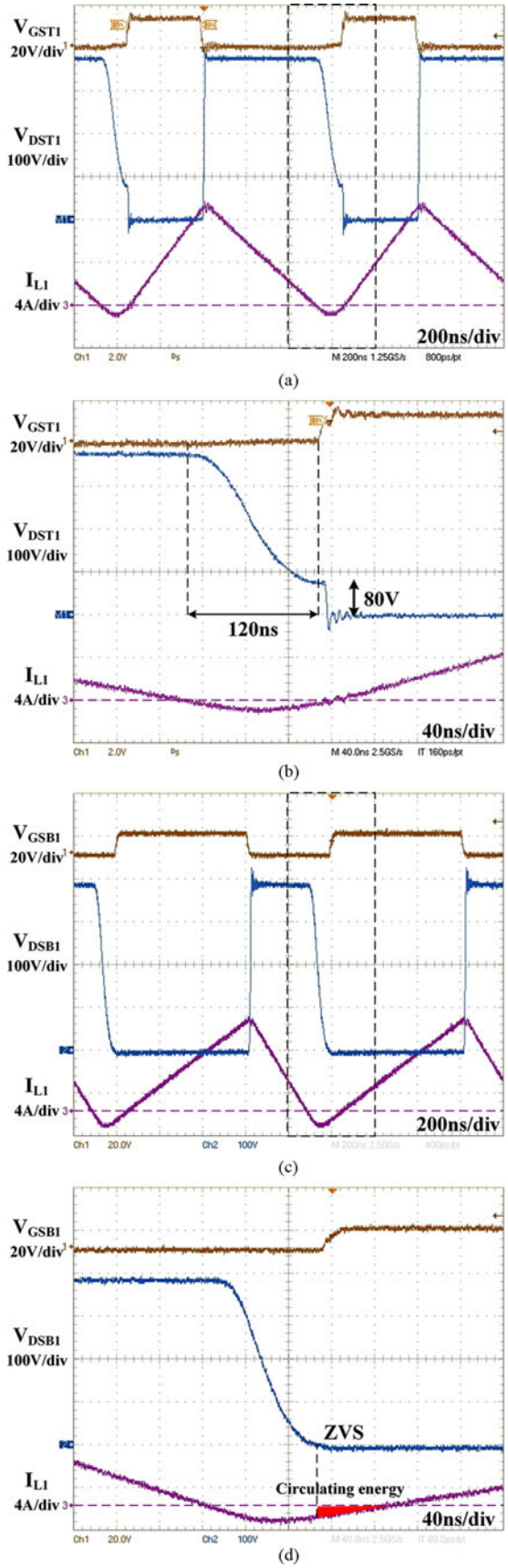

Fig. 15. Experimental waveforms of CRM operation with noncoupled inductor. (a) Buck direction. (b) Detailed resonant period. (c) Boost direction. (d) Detailed resonant direction.

energy induces roughly 0.5-W extra conduction loss at 1 MHz. The resonant period of the buck direction measured from the waveform is about 120 ns. It is shorter in the boost direction since the inductor voltage is clamped by V_b after the main switch achieves ZVS. The rms value of the inductor current is 5.2 A for both direction.

Fig. 16 shows the bidirectional waveforms with an inverse coupled inductor. The detailed waveforms during resonant period for the buck and boost direction are shown in Fig. 16(b) and (d), respectively. Fig. 16 clearly shows the ZVS achievement for the buck direction and a circulating energy reduction for the boost direction with a coupled inductor. The theoretical resonant period reduction according to Fig. 11 is about 15% with a coupled inductor. The resonant period measured from the waveform is about 100 ns, which matches with the theoretical analysis. The rms value of inductor current is 5 A for both direction, which reduces 4% compared with noncoupled case. The measured efficiency at full load output with a coupled inductor for both directions is 98.5%.

The loss breakdown of two-phase buck direction at full load is shown in Fig. 17. It clearly shows that the coupled inductor eliminates the turn on switching loss by ZVS range extension. Moreover, coupled inductor slightly reduce the conduction loss due to small reduction of rms current as mentioned in Fig. 12. Core loss is also reduced with coupled inductor since core volume can be shrink due to certain dc flux cancelation. Overall, the coupled inductor saves about 4-W power loss and improves efficiency by 0.3% at full-load condition. It should be pointed out that the inductor is not optimized in terms of losses, and therefore, there is still a room to improve the efficiency.

The full load range efficiency of buck direction is shown in Fig. 18. The efficiency of boost direction is similar. The switching frequency increases when the load current reduces due to the nature of CRM operation. The switching related loss becomes the dominant part at light-load condition. Therefore, the coupled inductor saves more loss at light load and the efficiency improvement is over 2%.

VI. Conclusion

This paper aims to analyze the benefits of the inverse coupled inductors in CRM operation based on a 1-MHz interleaved buck/boost converter with GaN devices. The converter behavior during the resonant period is improved with an inverse coupled inductor. There is a reduction of the resonant period, an extension of the ZVS range when $D < 0.5$, and a reduction of the circulating energy when $D > 0.5$. All of these characteristics are beneficial for high-frequency operation in terms of conduction and switching loss reduction. The coupled inductor prototype efficiency is 98.5% at 1 MHz, which is 0.3% higher than the efficiency of the noncoupled inductor, which validate the theoretical analysis.

Although this is not covered in this paper, it is worth pointing out that the coupled inductor provides a potential opportunity for magnetic integration. With dc flux cancellation, the coupled inductor could be further integrated, which would increase the power density. The authors are planning to continue exploring

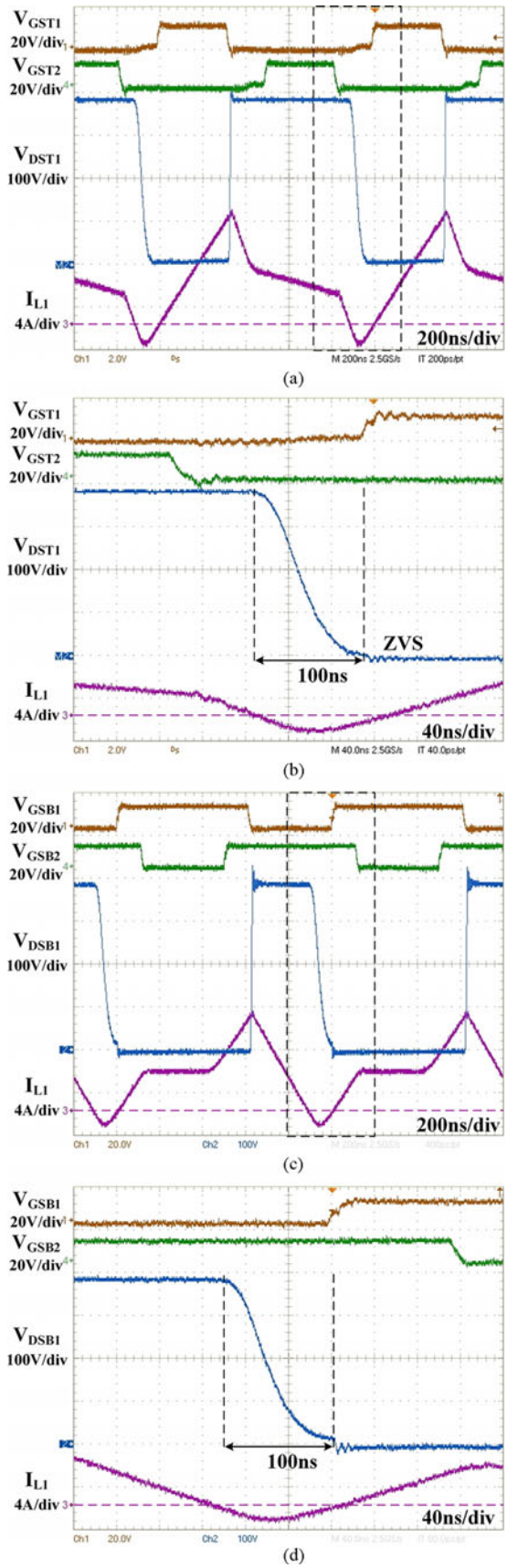

Fig. 16. Experimental waveforms of CRM operation with coupled inductor. (a) Buck direction. (b) Detailed resonant period. (c) Boost direction. (d) Detailed resonant period.

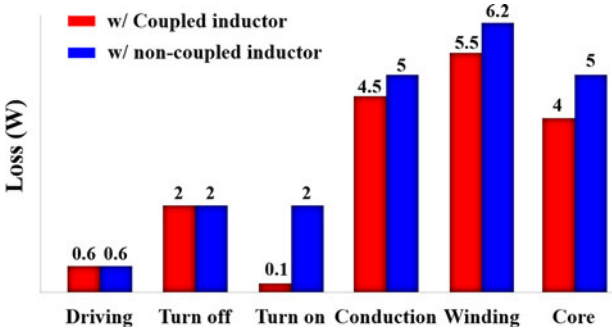

Fig. 17. Loss breakdown of two-phase buck direction at full load.

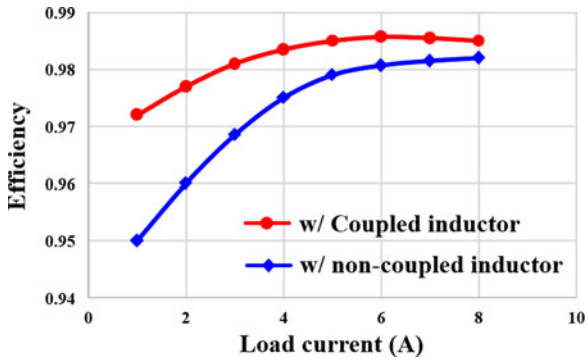

Fig. 18. Efficiency comparison over wide load range of buck direction.

the benefits of the coupled inductor and will consider for future publications covering the design and optimization of the coupled inductor in details.

ACKNOWLEDGMENT

The authors would like to thank Transphorm, Inc., for providing the GaN device samples.

REFERENCES

[1] O. Hegazy, R. Rarrero, J. V. Mierlo, P. Lataire, N. Omar, and T. Coosemans, "An advanced power electronics interface for electric vehicles applications," *IEEE Trans. Power Electron.*, vol. 28, no. 12, pp. 5508–5521, Dec. 2013.

[2] M. A. Khan, A. Ahmed, I. Husain, Y. Sozer, and M. Badawy, "Performance analysis of bidirectional DC-DC converters for electric vehicles," *IEEE Trans. Ind. Appl.*, vol. 51, no. 4, pp. 3442–3452, Jul./Aug. 2015.

[3] H. F. Ahmed, H. Cha, S. Kim, D. Kim, and H. Kim, "Wide load range efficiency improvement of a high-power-density bidirectional DC-DC converter using an MR fluid-gap inductor," *IEEE Trans. Ind. Appl.*, vol. 51, no. 4, pp. 3216–3226, Jul./Aug. 2015.

[4] W. Zhang, D. Dong, I. Cvetkovic, F. C. Lee, and D. Boroyevich, "Lithium-based energy storage management for DC distributed renewable energy system," in *Proc. IEEE Energy Convers. Congr. Expo.*, 2011, pp. 3270–3277.

[5] J. Baek, W. Choi, and B. Cho, "Digital adaptive frequency modulation for bidirectional DC-DC converter," *IEEE Trans. Ind. Electron.*, vol. 60, no. 11, pp. 5167–5176, Nov. 2013.

[6] M. A. Khan, G. Simin, S. G. Pytel, A. Monti, E. Santi, and J. L. Hudgins, "New developments in gallium nitride and the impact on power electronics," in *Proc. IEEE Power Electron. Spec. Conf.*, 2005, pp. 15–26.

[7] N. Kaminski, "State of the art and the future of wide band-gap devices," in *Proc. IEEE Power Electron. Appl.*, 2009, pp. 1–9.

[8] Z. Liu, X. Huang, M. Mu, Y. Yang, F. C. Lee, and Q. Li, "Design and evaluation of GaN-based dual-phase interleaved MHz critical mode PFC converter," in *Proc. IEEE Energy Congr. Expo.*, 2014, pp. 611–616.

[9] D. Huang, A. Ji, and F. C. Lee, "LLC resonant converter with matrix transformer," *IEEE Trans. Power Electron.*, vol. 29, no. 8, pp. 4339–4347, Aug. 2014.

[10] D. Reusch and J. Strydom, "Evaluation of gallium nitride transistor in high frequency resonant and soft-switching DC-DC converters," *IEEE Trans. Power Electron.*, vol. 30, no. 9, pp. 5151–5158, Sep. 2015.

[11] X. Huang, Z. Liu, F. C. Lee, and Q. Li, "Characterization and enhancement of high-voltage cascode GaN devices," *IEEE Trans. Electron. Devices.*, vol. 62, no. 2, pp. 270–277, Feb. 2015.

[12] X. Huang, Q. Li, Z. Liu, and F C. Lee, "Analytical loss model of high voltage GaN HEMT in cascode configuration," *IEEE Trans. Power Electron.*, vol. 29, no. 5, pp. 2208–2219, May 2014.

[13] X. Huang, Z. Liu, Q. Li, and F C. Lee, "Evaluation and application of 600 V GaN HEMT in cascode structure," *IEEE Trans. Power Electron.*, vol. 29, no. 5, pp. 2453–2461, May 2014.

[14] Z. Liu, X. Huang, F. C. Lee, and Q. Li, "Package parasitic inductance extraction and simulation model development for the high-voltage cascode GaN HEMT," *IEEE Trans. Power Electron.*, vol. 29, no. 4, pp. 1977–1985, Apr. 2014.

[15] P. Wong, Q. Wu, P. Xu, Y. Bo, and F. C. Lee, "Investigating coupling inductors in the interleaving QSW VRM," in *Proc. IEEE Appl. Power Electron. Conf.*, 2000, pp 973–978.

[16] F. Wang, X. Ruan, Y. Yang, and Z. Ye, "Interleaved critical current mode boost PFC converter with coupled inductor," *IEEE Trans. Power Electron.*, vol. 26, no. 9, pp. 2404–2413, Sep. 2011.

[17] V. Vorperian, "Quasi-square-wave converters: Topologies and analysis," *IEEE Trans. Power Electron.*, vol. 3, no. 2, pp. 183–191, Apr. 1988.

[18] G. Hua and F. C. Lee, "Soft-switching techniques in PWM converters," *IEEE Trans. Ind. Electron.*, vol. 42, no. 6, pp. 595–603, Dec. 1995.

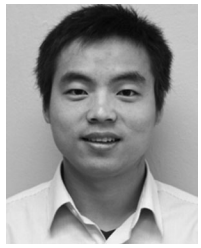

Xiucheng Huang (S'12) was born in Zhejiang, China, in 1986. He received the B.S. and M.S. degrees in electrical engineering from Zhejiang University, Hangzhou, China, in 2008 and 2011, respectively. He is currently working toward the Ph.D. degree at the Center for Power Electronics Systems, Virginia Tech, Blacksburg, VA, USA.

His main research interests include high-frequency high-power density power conversion, soft-switching technique, and power architecture.

Fred C. Lee (S'72–M'74–SM'87–F'90–LF'12) received the B.S. degree in electrical engineering from the National Cheng Kung University, Tainan, Taiwan, in 1968, and the M.S. and Ph.D. degrees in electrical engineering from Duke University, Durham, NC, USA, in 1972 and 1974, respectively.

He is currently a University Distinguished Professor at Virginia Polytechnic Institute and State University, Blacksburg, VA, USA, where he is the Founder and Director at the Center for Power Electronics Systems. He holds 72 U.S. patents, and has published 252 journal articles and 639 refereed technical papers.

Dr. Lee has served as the President of the IEEE Power Electronics Society from 1993 to 1994. He received the William E. Newell Power Electronics Award in 1989, the Arthur E. Fury Award for Leadership and Innovation in 1998, the Honorary Sun Yuen Chuan Chair Professor at National Tsinghua University, Taiwan, in 2001, the Outstanding Alumni Award from National Cheng Kung University in 2004, the Ernst–Blickle Award for achievement in the field of power electronics in 2005, and the Honorary Kwoh-Ting Li Chair Professor Award at National Cheng Kung University, Taiwan, in 2011. He is a Member of the National Academy of Engineering, USA, and an Academician of Academia in Taiwan.

Qiang Li (M'11) received the B.S. and M.S. degrees in power electronics from Zhejiang University, Hangzhou, China, in 2003 and 2006, respectively, and the Ph.D. degree from Virginia Tech, Blacksburg, VA, USA, in 2011.

He is currently an Assistant Professor at the Center for Power Electronics Systems, Virginia Tech. His research interests include high-density electronics packaging and integration, high-frequency magnetic components, and high-frequency power conversion.

Weijing Du was born in Shanxi, China, in 1985. She received the B.S. and Ph.D. degrees from the Department of Electrical Engineering, Zhejiang University, Hangzhou, China, in 2008 and 2013, respectively. She is currently a Visiting Scholar at the Center for Power Electronics Systems, Virginia Tech, Blacksburg, VA, USA.

Her current research interests include high-frequency high-density power converters and gallium nitride device applications.